IOP Publishing
PostPrint of Supercond. Sci. and Techn. **33 (2020) 08500** https://doi.org/10.1088/1361-6668/ab9520

MgB_2 cables made of thin wires manufactured by IMD process

P. Kováč[1*], L. Kopera[1], M. Hain[2], E. Martínez[3], J. Kováč[1], T. Melišek[1], D. Berek[1] and I. Hušek[1]

[1]Institute of Electrical Engineering, Slovak Academy of Sciences, Dúbravská cesta 9, 841 04 Bratislava, Slovakia
[2]Institute of Measurement Science, Slovak Academy of Sciences, Dúbravská cesta 9, 841 04 Bratislava, Slovakia
[3]Instituto de Ciencia de Materiales de Aragón, CSIC-Universidad de Zaragoza, C/María de Luna 3,E-50018 Zaragoza, Spain
[*]Corresponding author: Pavol.Kovac@savba.sk

Received 3 April 2020
Accepted for publication 20 May 2020
Published 22 June 2020

Abstract

This paper presents the properties of cables made of thin MgB_2 wires with different sheaths manufactured by IMD process. Strong effect of the outer sheath on the $J_e(B)$ performance was observed and the best properties were obtained for the strongest Cu sheath. It was found that the transversal and longitudinal cables uniformity affects the critical currents in MgB_2 wires made by IMD considerably. We have analyzed the quench dynamics in Rutherford cables with Al+1.5%$A_{l2}O_3$ sheath, when subjected to heat disturbances. Quench triggered in the strands in direct contact with the heater, observing important delays in quench development among strands. Low AC losses were measured for the extra-light Rutherford cable with Ti barrier and Al+1.5%Al_2O_3 sheath due to an increased barrier resisitivity and surface Al sheath oxidation, which reduces coupling current loss component effectivelly.

Keywords: thin MgB_2 wires, IMD process, circular and flat cables, uniformity, critical currents, quench dynamics, AC losses

1. Introduction

It has been observed, that the superconducting properties of multi-filamentary MgB_2 wires vary with the diameter of filaments and their minimum size is in the range of tens to hundred microns [1]. It is due to a strong compaction of the precursor powder leading to a sausaging effects for restacked filamentary MgB_2 wires where the deformation ratios are considerably higher than for single-core ones [2]. Especially conductors with fine precursor powders, like extensively milled or mechanically alloyed powders, often suffer from sausaging effects [3]. The resulting variations in filament diameter along the conductor lead to reduced current carrying capability and sometimes also to the formation of cracks in the sheath material [3]. During the deformation process into thin filaments a large and hard grains could easily cause a crack if it gets close to the sheath material, whereas in a large filament it could be surrounded by smaller or softer material, thus preventing a damage of the sheath material during deformation. Consequently, applied manufacturing processes (Power-in-Tube: *ex-situ* or *in-situ* and IMD: internal magnesium diffusion) have an apparent effect on in-length uniformity of manufactured MgB_2 wires. While well mixed powders used by PIT approach makes it possible to obtain uniform filaments [1], metallic Mg core surrounded by boron powder in IMD process may lead to an apparent variation of magnesium core and consequently to a strong differences in properties along the wire. In other words, MgB_2 wires fabricated by IMD processes have much higher potential in local critical current than the global value estimated by the four-probe transport method [4].

The increased number of deformation steps necessary to achieve thin wires leads also to work hardening of the metallic sheath. This can cause cracks in the sheath material if no heat treatments are applied to release the stresses. On the other

hand, work hardening of the sheath can enhance the density of powder and also the final tolerance of the wire against tensile stresses. However, this strongly depends on the applied sheath material and the temperature of the final heat treatment.

Some superconducting devices require higher currents than can be carried by single wires, which leads to the request for cables assembling. In addition, a transposition of the strands is also desirable to reduce AC losses. For cabling purposes, *in situ* MgB_2 wires seems to be the best candidates to realize a transposition of strands, allowing hard bending before reaction treatment without damage. Unreacted wires can be bent to very small bending radii [5-9]. In contrast to *in situ*, the use of *ex situ* wires is limited by their bending behaviour when being assembled into cables [10-11]. Recently, Rutherford MgB_2 cables were also made by using unreacted *in-situ* [12] and IMD wires [13]. AC losses in these cables can be suppressed effectively by increased inter-strand resistivity [14]. To avoid a strong degradation of the transport currents, better way is to made cables of thin wires with one ore small number of filaments. Balancing the final properties of a cable to an optimum is still a challenge and requires systematic work to control the different parameters.

In this study, single-core MgB_2 composites with different metallic sheaths made by the IMD process were drawn into a small wire diameters ~ 0.4 mm. As-deformed wires were used for circular 7- and flat 12- strands cables subjected to: densification, heat treatment and transport current measurements. Quench dynamics and AC losses of extra-light 12- strands Rutherford cable were also analysed.

2. Experimental

The set of single-core MgB_2 wires has been made by identical IMD process. The metallic tubes with purity 99.9% of diameter 9.0/6.2 mm were used for outer sheath: from Cu (named Cu-A) and from Al with 1.5 vol % Al_2O_3 metal matrix composite (named Al-B) and Al with 3.1 vol % Al_2O_3 (named Al-C) prepared by powder metallurgy [15-17] are described by Table 1. HV0.05 is the micro-hardness measured for these sheath materials in as-deformed state.

Table 1. Cu and Al+Al_2O_3 sheath materials used for MgB_2 wires.

Metallic sheath	Cu-A	Al-B	Al-C
Metal purity [%]	99.9	99.9	99.9
Al_2O_3 [vol. %]	-	1.5	3.1
HV0.05 [MPa]	125	70	90

V 99.95 % or Ti 99.99 % tubes of purity and the outer diameter 6.0 mm were selected for diffusion barrier in which a pure Mg rod of diameter 2.9 mm was centrally inserted. Comparable micro-hardness HV0.05 ~ 200 MPa were measured for as-deformed Ti and V. The space between the Mg rod and the barrier tube was filled by boron powder of purity 99.8 % and < 1 µm grain size. The assembled composite wires were groove rolled down to 2.2 mm and then were drawn into wires (wA, wB and wC) of minimal diameter 0.389 mm with several intermediate annealings at 320 ºC/30min for wA of diameters 1.27 mm, 0.952 mm and 0.716 mm and at 450 ºC/30min for wB and wC at diameter 1.33 mm, 0.952 mm, 0.665 mm and 0.500 mm. Circular cables (1+6) (named Cc-A, Cc-B, and Cc-C) of outer diameter d_{cable} =1.2 mm have been made from seven Cu sheathed V barrier wire wA of diameter 0.389 mm and two Al sheathed Ti barrier wires (wB and wC) of the same size, see Table 2. Short cable samples were densified by rotary swaging deformation down to 1.1 mm and to 1.0 mm diameter.

Flat 12 strands Rutherford cable of 0.86 mm x 2.86 mm (Rc-B) were braided only from the wB strands of 0.448 mm with the transposition length L_p ~ 26 mm. Short sample of Rc-B cable was additionally also densified by rolling to the size of of 0.82 mm x 2.78 mm. Rc-B of 0.86 mm was also insulated by anodic oxidisation in 5 % liquid of oxalic acid ($C_2H_2O_4$) with the current density 0.1 Acm^{-2} for 30 min. It results in ~ 15 µm thick Al_2O_3 layer at the outer cable surface. Cross-sections of cable samples were examined by the Olympus BX51M optical microscope and cables uniformity more in details by X-ray tomography, see Figure 1.

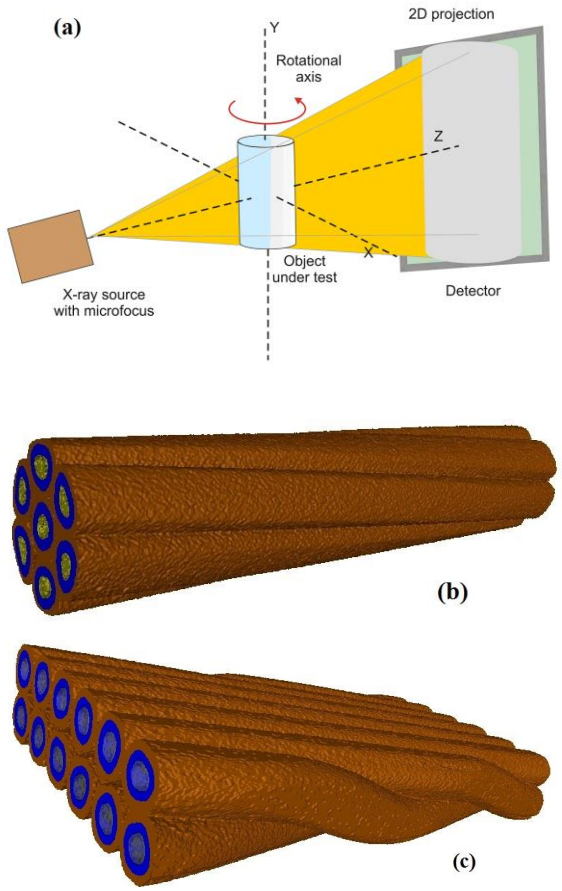

Figure 1. Arrangement of X-ray tomography (a) 3D view of 7 strands (b) and 12 strands Mg/B/Ti/Al+Al_2O_3 Rutherford cable (c).

X-ray micro-tomography measurement device Nanotom 180 equipped with nano-focusing X-ray tube and maximal accelerating voltage 180 kV was used for non-destructive analysis. Cable samples under test were stepwise turned around the rotation axis at a small selected angle (e.g. 15' and rotated totally at 360 °) and so called X-ray projections were measured. After obtaining all necessary projections the volume image was constructed based on the inverse Radon transformation and resulting 3D image allows observing well the composite uniformity.

The final heat treatment of all circular cables was done under argon atmosphere at temperature 645 ºC for 30 min and at 642 ºC/35min or 635 ºC/15min for Rc-B Rutherford cable. Transport critical currents were measured at liquid He temperature and external magnetic field between 2.0 T and 8.0 T using standard DC measurement with 1 μVcm^{-1} criterion.

Quench measurements were performed for the flat cables Rc-B of 2.86 mm x 0.86 mm (w x d), total length of about 11 cm (≈ 8 cm between current contacts) using a similar set-up and procedure as described in [18]. The cable was in vacuum, cooled by conduction from both current contacts and the energy was deposited into the cable by passing current pulses of variable duration, t_p, in a heater of resistance 120 Ω, which was glued on one of the sides of the cable and overlays five strands. A Hall sensor placed at about 2 mm of the cable edge measures the magnetic field in the direction perpendicular to the cable plane (w x L), in order to analyse the self-field changes during a quench [19]. A thermocouple and several voltage taps were soldered along the cable in individual strands, so that it is possible to measure intra-strand and inter-strand voltages (i.e. between two taps in the same strand and in different strands, respectively). In the experiments, all voltages are always measured using the same polarity, left–right, in such a way that in the normal state all measured voltages are positive.

AC losses in Rutherford MgB_2 cable with and without Al_2O_3 insulating layer were measured by the system based on the calibration free method [20]. External magnetic field was oriented perpendicular to the plane of cable sample. The temperature was ranged from 18 K up to 40 K.

3. Results and discussion

3.1. Critical currents

Critical currents of Al sheathed wB wire of different diameters (from 0.8 mm to 0.398 mm) were measured at liquid He temperature and external magnetic fields 2-8 T. Figure 2 shows the dependence of engineering current density (J_e) versus the wire diameter (d_w), where an apparent degradation of J_e is observed for wB wire at $d_w < 0.448$ mm. While J_e(5T) of wB wire at diameter 0.8 mm is ~ 10^4 Acm^{-2}, it is reduced by one order of magnitude at 0.389 mm. Surprisingly, J_e of Cu sheathed wA wire is by more than one order of magnitude higher in comparison to wB at the same diameter 0.389 mm.

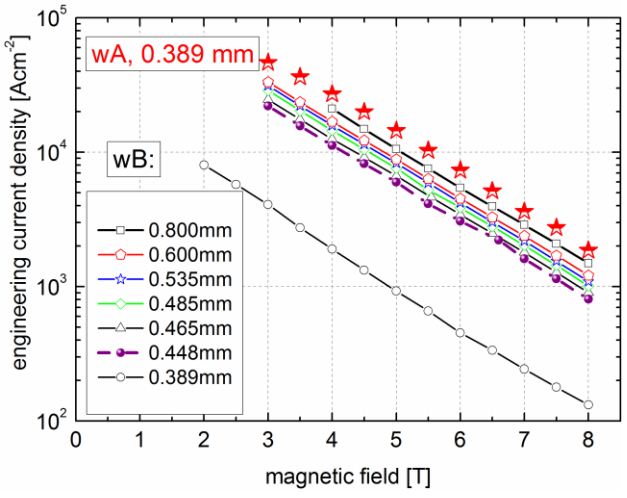

Figure 2. Engineering current densities of wB wire with different diameters and wA of 0.389 mm annealed at 645 ºC /30min.

Table 2. Circular cables (1+6) made of MgB_2 wires wA-wC of 0.389 mm.

Cable	Cc-A	Cc-B	Cc-C
Sheath	Cu	Al+1.5%Al_2O_3	Al+3.1%Al_2O_3
Barrier	V	Ti	Ti
Diameter	1.0-1.2mm	1.0-1.2mm	1.0-1.2mm

Critical currents of circular cables Cc-A, Cc-B and Cc-C are ploted by Figure 3. Figure 3(a) shows critical currents for Cc-A of diameters 1.2 mm, 1.1 mm and 1.0 mm compared with the critical current of wA wire multiplied by 7, which demonstrate a small degradation (~23 %) by cabling. The engineering current density for Cc-A cables were calculated as the ratio of critical current to the cable cross-section and J_e = 10^4 Acm^{-2} were obtained for the following values of magnetic fields: 4.9 T for 1.2 mm, at 5.1 T for 1.1 mm and at 5.7 T for 1.0 mm cable, which is even better than for single wA wire of 0.389 mm shown by Figure 2 (10^4 Acm^{-2} at 5.5 T). The best $J_e(B)$ for Cc-A 1.0 mm represents an improvement of J_e by 77 % in comparison to Cc-1.2 mm. Apparent are also changes in n-values, which are quite similar for 1.2 mm and 1.1 mm (~ 20 at 3.5 T), but considerably improved for 1.0 mm cable (~ 100 at 3.5 T).

Figure 3(b) presents the critical currents of cable Cc-B of diameters 1.0-1.2 mm, which show different behaviour in comparison to Cc-A and also much lower currents. Critical currents of 1.2 mm cable compared to the sume current of seven strands indicates more radical degradation by cabling (~ 47 %) than for Cc-A (23 %). One can see that swaging of this cable to 1.1 mm has changed the slope of $I_c(B)$ characteristic and the n-exponent is lowered as well. Furher densification by swaging to 1.0 mm has resulted in an increase $I_c(B)$ and n-exponent, but calculated J_e = 10^4 Acm^{-2} is measured at

relativelly low external field of ~ 3.0 T. The best characteristics of Cc-B were also measured for 1.0 mm in diameter.

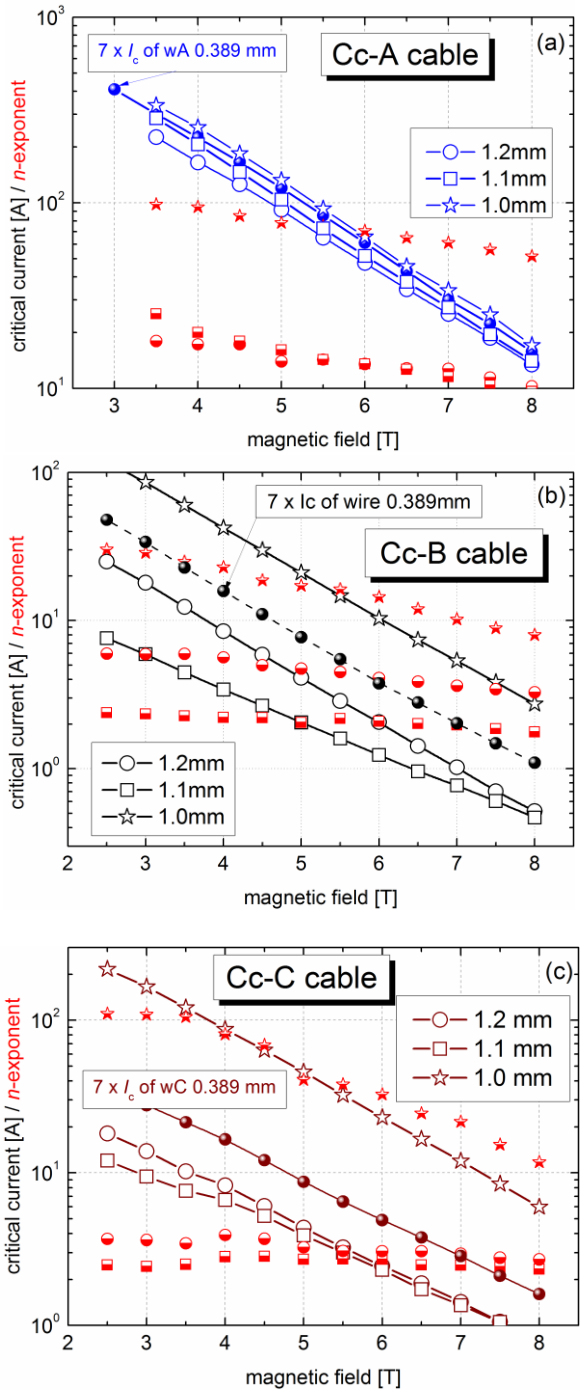

Figure 3. Critical currents and *n*-exponents of circular cables Cc-A (a), Cc-B (b) and Cc-C (c).

Figure 3(c) presents the critical currents and *n*-exponents of Cc-C with low I_c and *n* values for diameters 1.2 and 1.1 mm. But, improvement by one order of magnitude is well visible for this cable swaged down to 1.0 mm. This cable shows better performanece than Cc-B but much worse than Cc-A. As shown by Figure 3, the *n*-exponent follows the changes of the critical current with nearly the same behaviour in all dependences presented. Meaning of *n*-exponent has been described by Seeber B [21] and by Fabbricatore P et al using of formula $n(B,t)=U_0(B)g(t)/k_BT$ [22], where k_BT is activation energy and U_0 is pinning potential. The determination of $n(B,t)$ was done from the *I-V* curves measured MgB_2 wires at a constant temperature [22]. The ratio of I_c/n was also analyzed in details for Bi-2223/Ag superconductors and it was shown that the higher the I_c/n ratio the better structural quality reflecting the effective number of inter-grain connections and pinning centers [23]. Consequently, *n* values of presented samples represent intrinsic pinning energy and also extrinsic quality e.g. wires uniformity affecting the slope of measured *I-V* characteristics. Low *n* and I_c are typical for as-braided or slightly densified cables (1.2 mm and 1.1 mm), but increased *n* is evident for well densified cables (1.0 mm). Dense boron allows to create MgB_2 phase with well-connected grains and also with better wire's uniformity. Due to low density of boron in as-drawn wires of circular cables 1.2 mm, the created MgB_2 phase has lower current density in comparison to those where boron density is increased by additional deformation by rolling, swaging or pressing. This effect has been already shown for MgB_2 cable made of in-situ wires by Holubek [7] or Hossain [24].

Engineering current densities of Cc-A, Cc-B and Cc-C of the same diameter 1.0 mm are compared in Figure 4. One can see, that $J_e = 10^4$ Acm^{-2} is measured at fields between 3.0 and 5.7 T and the best performance is evident for Cu sheathed cable Cc-A. Engineering current densities corelate well with the hardness of used outer sheath (see Table 1), which should influences the density of Boron powder during the wire drawing and consequently affects the formation of dense MgB_2 phase positivelly [7, 24].

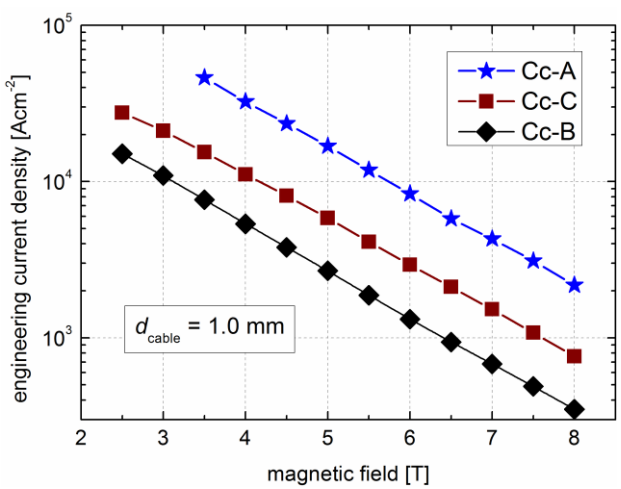

Figure 4. The best engineering current densities of cables Cc-A, Cc-B and Cc-C annealed at 645 °C /30min

3.2. *Cables uniformity*

Figure 5 shows the cross-sections of circular cables Cc-A – Cc-C of the same diameter 1.1 mm. While quite uniform strands were observed for Cu sheathed cable Cc-A, varying strand sizes and also core densities (bright colour represents higher density and dark one lower) are seen for Al sheathed cables Cc-B and Cc-C. Thicker and regular V-barrier but also some leafing of Cu stabilzation is observed for the outer

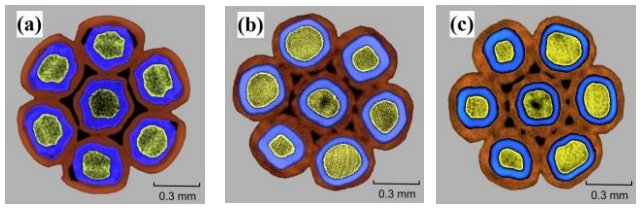

Figure 5. The cross-sections of circular cables of outer diameter 1.1 mm: Cc-A (a), Cc-B and Cc-C (c) obtained by X-ray micro-tomography. Blue colour is attributed to V or Ti barriers and red one to outer sheaths.

strands of Cc-A cable, see Figure 5(a). Any leafing of Al sheath but variable thickness of Ti with no barrier breaking were observed in Cc-B and Cc-C cables at 1.1 mm, see Figures 5(b) and 5(c). Figure 6 compares the longitudinal uniformity for cable's central strands, which is the best one for Cc-A. Apparent irregularities (sausaging effect) are well visible in Cc-B and Cc-C for inner composite elements (Mg, B and Ti). While the possition of Mg in the axis of Cc-A strand is not well visible, dark colour in Cc-B and Cc-C strands corresponding to lower density Mg in comparison to more dense boron powder. It is due to smaller X-ray absorption by more porous and/or lower concentration of elements with higher nucleon number. Comparison of Cc-C with Cc-B indicates higher boron density for Cc-C, which may be a reason of harder outer sheath used for this wire, see Table1.

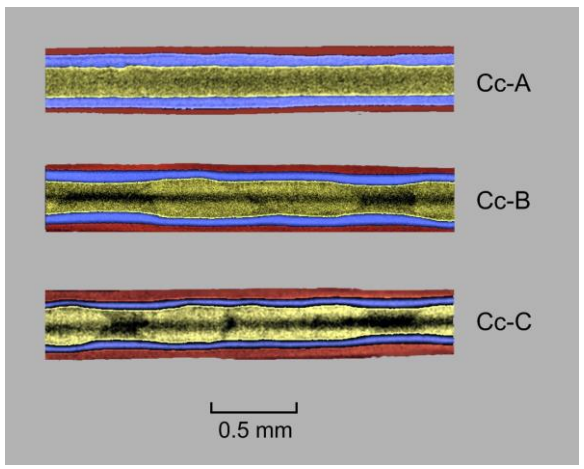

Figure 6. The longitudinal views of the central wires of cables Cc-A, Cc-B and Cc-C of diameter 1.1 mm obtained by X-ray micro-tomography.

3.3. *Rutherford cable*

To avoid an apparent critical current degradation for thin wB strands (see Figure 2), Rc-B cable has been made from 12 wires of diameter 0.448 mm, see Figure 7. Cross-section of not annealed Rc-B cable observed by optical microscopy is shown by Figure 7(a), where quite uniform individual strands are visible. But, the polishing of soft Al+Al_2O_3 sheath and esspecially the central Mg-core effects lightly the view of individual strands and their main components. Figures 7(b) show more uniform strands observed for Rc-B cable by X-ray micro-tomography, but, similarly as for Cc-A cable it is not possible to distinguish clearly the difference between Mg core and surrounding boron layer. Figure 7(b) shows also a place of broken Ti barrier at the cable edge.

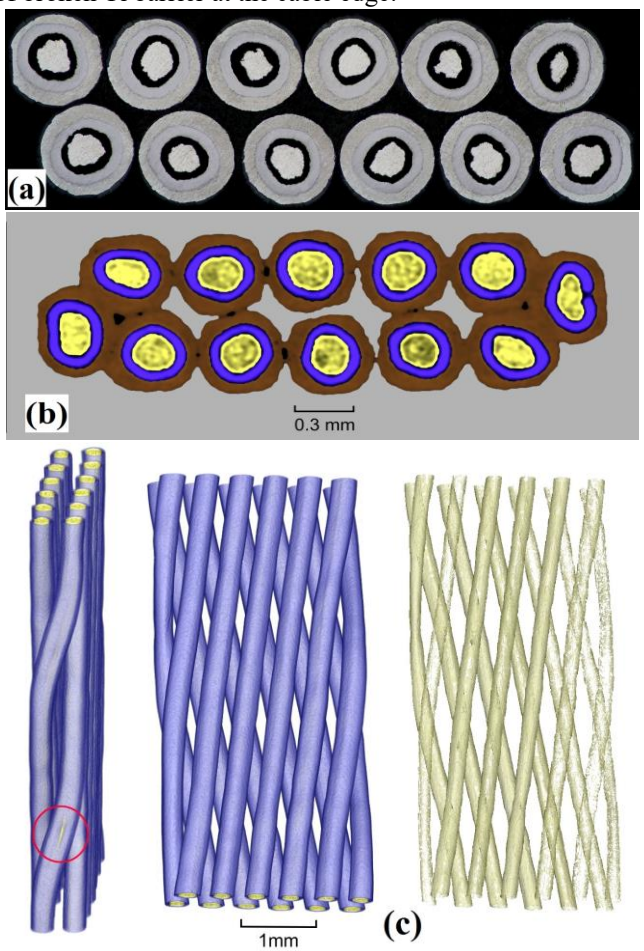

Figure 7. Cross-section of Rc-B cable 2.86 x 0.86 mm observed by optical microscopy (a) and by X-ray tomography showing also more deformed edge strands (b). 3D views of Rc-B without Al sheath and also with taken out Ti barriers (c).

It means that higly deformed Ti is not more ductile enough material and can be interupted at the places of extreme deformation – rolled cable edges. Figure 7(c) shows 3D views of Rc-B cable with removed Al+Al_2O_3 sheaths and also without Ti barriers (by post-processing in the software VG

StudioMAX 2.1). The position of most probably breaking of Ti-barrier at the cable edge is marked by red circle. Next 3D view from the flat side of cable show very uniformly shaped Ti barriers of diameter ~ 0.3 mm for all 12 strands, but not the same densities for strands placed at cable edges and at the cable centre. The mechanical deformation is the highest at cable edge parts and consequntly the boron powder is by ~ 40 % denser there.

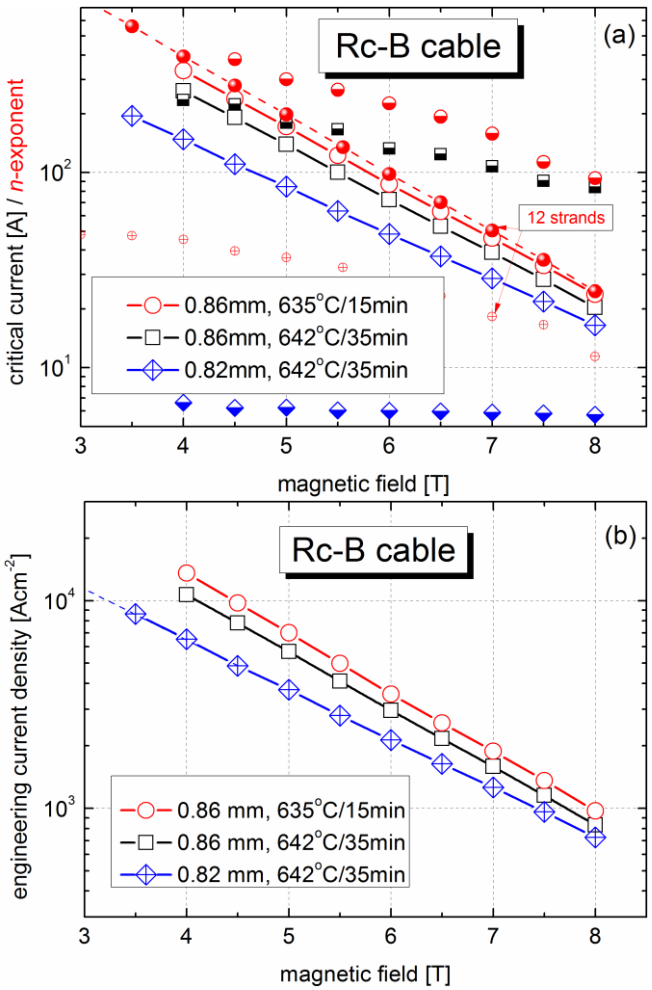

Figure 8. Critical currents and *n*-exponents (a) and engineering current densities (b) of three Rc-B samples.

Figure 8 shows the transport current properties of Rc-B cable of thickness 0.86 mm and 0.82 mm annealed at two regimes. Comparison of cable critical current with 12 strands shows only small degradation by cabling is shown by Figure 8(a). Aditional rolling deformation of this cable from 0.86 mm to 0.82 mm has decreased $I_c(B)$ and reduced *n*-exponent radically, which can be caused by broken barrier as shown by Figure 7(c). Rc-B cable of 0.86 mm has higher critical currents and also high *n*-exponents ~ 10 times larger than for individual wB strand of 0.448 mm. Figure 8(b) compares the corresponding engineering current densities of Rc-B samples crossing the level of $J_e = 10^4$ Acm^{-2} between the fields 3.2 and 4.5 T, which is still lower value in comparison to Cc-A cable with copper sheath. It can be attributed to mechanically softer Al+Al_2O_3 sheath used for Rc-B cables.

3.3. Quench in Rc-B Rutherford cables

In order to analyse the quench behaviour of Rc-B cables, the heater was glued at mid distance between the current contacts. Upon cooling the sample to the operation temperature, a current (*I*) lower than the critical one is applied. Then, the energy deposited is incremented in small steps (in several runs) by increasing the duration of the heat pulse, until a quench develops, which causes the transition from superconductor to normal of the whole cable.

Figure 9 shows the voltages and the temperature measured in the region around the heater during a quench. For clarity purposes, two strands have been highlighted in Figure 9(a): strand A has a segment in direct contact with the heater and B is symmetrically disposed but in the opposite side of the cable. After applying the heat pulse, the temperature of the strand segment in contact with the heater increases and enters in the current-sharing regime, which results in the generation of voltage [25, 26].

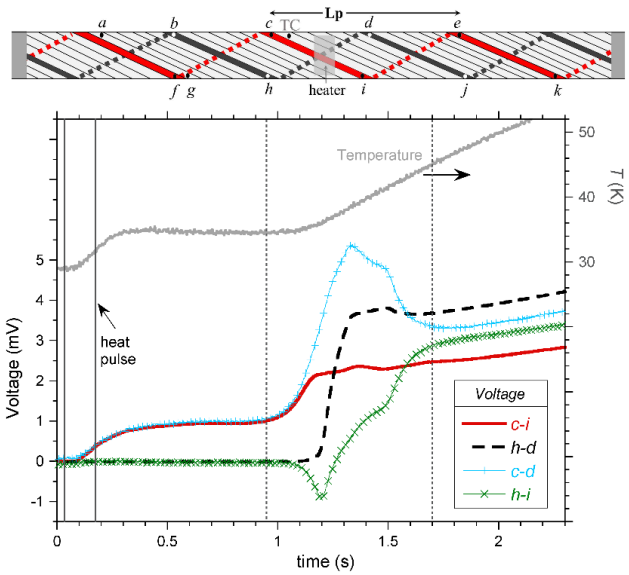

Figure 9. Scheme of the measured Rc-B Rutherford cable with installed voltage taps *a, b… k*, thermocouple (TC) and heater. Two strands named A (red) and B (black) are highlighted. Bellow is the temperature measured by thermocouple TC and voltages meaured between different taps in the region around the heater at $T = 29$ K and $I = 75$ A ($I/I_c \approx 0.75$), when a heat pulse of 110 mJ is applied.

At the time $t \approx 0.95$ s the system becomes unstable and quench triggers in strand A whereas strand B is still superconducting. Note that the temperature measured by thermocouple TC, which was attached close to tap *c* but at the nearest strand, has similar behaviour than voltage *c-i* (with an expected small delay as it senses about 1 cm-long segment while the temperature is measured in a spot), thus suggesting that the quench triggers in several strands segments in contact with the

heater. The time delay between the transition of strands at the top of the cable and those at the bottom in the heater region is significant and causes strong differences between the inter-strand voltages *c*-*d* and *h*-*i*, and even negative values of the latter. Eventually, the transition to normal state of all the strands takes place, but note that it is not until $t \approx 1.7$ s, that all the zone around the heater limited by taps *c*, *d*, *h* and *i* becomes normal.

This behaviour has been observed for two nominally identical analysed cables. In order to further analyse the quench propagation in these cables, voltages generated during a quench along strands A and B were recorded for different heater configurations. Figure 10 shows the results for the heater placed in the centre of the cable. As explained before, quench initiates in the strands directly in contact with the heater (voltage A0) and propagates along this strand symetrically from the heater (voltages A1 and A1'). Thus, at $t \approx 1.25$ s (discontinous vertical line in the figure), the normal zone in strand A has already extended up to taps *f* and *e*, whereas for the strand underneath (B) just the segment bounded by taps *h* and *d* is in the normal state. The time delay between voltages was measured in the similar location of the cable but in these two opposite strands (voltages A1 and B1) is about 200 ms.

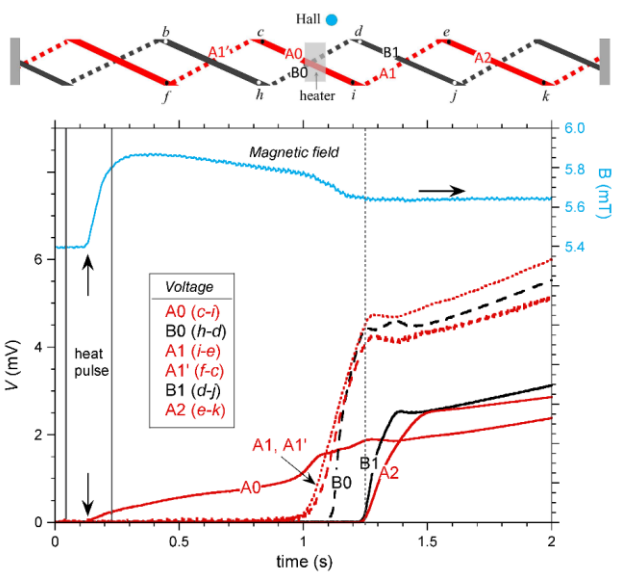

Figure 10. Voltages measured in different segments along strands named A and B (same cable as in figure 9), and magnetic field measured by the Hall sensor during a quench (applied energy of 156 mJ at $T = 27$ K and $I = 90$ A, $I/I_c \approx 0.67$). The different measured voltages are named as indicated in the scheme and label (just two strands have been drawn for claritiy purposes).

It is also observed that the magnetic field measured by the Hall sensor begins to increase just at the moment when voltage appears during the heat pulse ($t \approx$ 0.13 s in figure 10). The total current flowing through the cable, which was measured directly, remains constant during the experiment, thus indicating that current is redistributing among strands. It must be noted that the Hall sensor was located in the horizontal lower plane of the cable, so that the observed increment in the magnetic field would be consistent with an increase of the current flowing through the non-heated strands underneath. It is also observed that the measured self-field values for superconducting and normal states are different, which would indicate the presence of some inhomogeneities in the $E(J)$ characteristics among strands or strand's segments.

As the above configuration does not allow the experimental estimation of the quench propagation velocity, v_p, the same experiment was performed with the heater moved a distance approximately equal to the transposition pitch L_p from the centre, as shown in Figure 11.

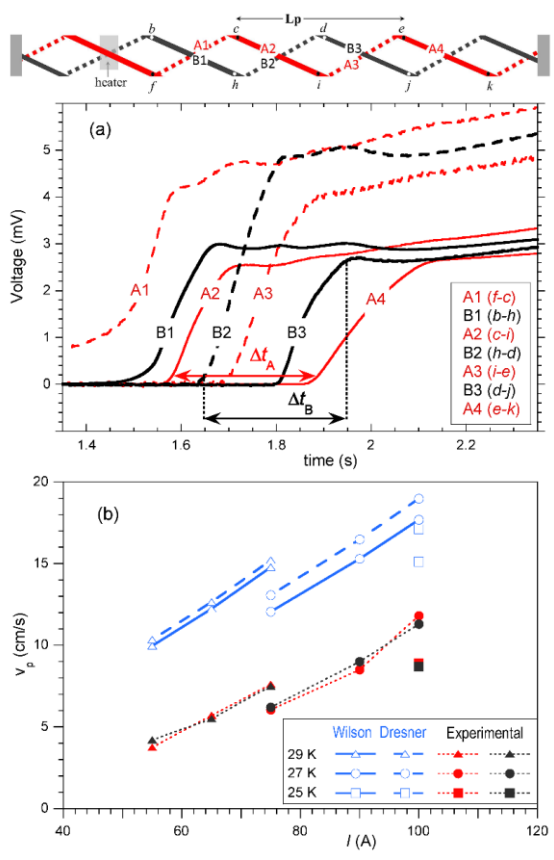

Figure 11. (a) Voltages measured during a quench along strands A and B (same cable, current and temperature as in figure 2) when the heater is placed at a distance Lp from the centre. The applied energy was 301 mJ. (b) Quench propagation velocities, v_p, as a function of the applied current at different temperatures: full symbols correspond to experimentally obtained values using equation (1); and open symbols to theoretical predictions by Wilson and Dresner models for 1D geometry.

Note that quench propagates similarly along strands A and B, but with a time delay between them. During the time interval between the onset of voltages A2 and A4 (Δt_A), the quench front in strand A moves from tap *c* to *e*, which are separated by a distance equal to Lp. Similarly, Δt_B gives the

time interval needed for the quench front in strand B to propagate from tap *h* to *j*, also separated by a distance Lp. Therefore, it is possible to estimate experimentally the propagation velocities as:

$$v_p = \frac{\mathrm{Lp}}{\Delta t} \quad \text{with} \quad \Delta t = \Delta t_{\mathrm{A}} \text{ or } \Delta t_{\mathrm{B}} \quad (1)$$

The values thus obtained are plotted as a function of the applied current and at different temperatures in figure 3(b). It is worth noting the good correspondence between them, although these values are much lower than those given by the analytical predictions for one-dimension geometry proposed by Wilson [25] and Dresner [27].

The behaviour of the cables analysed in this study under heat disturbances differs substantially from the results obtained in similarly manufactured MgB_2 Rutherford cables, but made with wires processed differently (PIT, in-situ reaction, Cu-Ni alloy sheath and Nb barrier [18]. Unlike for the R-c cables analyzed here, in the Rutherford cables made Cu-Ni sheathed PIT wires, the quench was found to trigger at the same time in all strands (those directly heated and those underneath), and the average quench propagation velocities estimated experimentally showed a close correlation with the prediction given by Wilson and Dresner modes, although with significant local variations of the quench propagation velocity near the hot-spot. It is still unknown if the different electrical resistivity (2.4×10^{-8} Ω m and 3.7×10^{-9} Ω m for cables made with CuNi and Al-Al_2O_3 sheathed wires, respectively) or the likely different electrical contact resistances between strands in both type of cables could be the reason of the observed differences.

3.4. AC losses of Rc-B cables

The surface views of Rc-B cable of thickness 0.86 mm heat trated at 635 ºC/15min before and after anodic oxidation are shown by Figure 12.

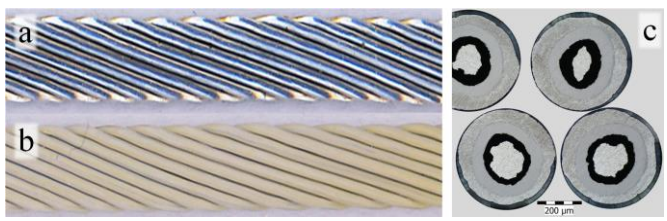

Figure 12. Outer surface of as-deformed (a) and oxidated (b) Rc-B cable and local view showing not uniformly insulated strands (c).

AC losses of Rc-B cables annealed at 635 ºC/15min were measured at variable temperatures and frequencies. Figure 13(a) shows the temperature dependences of AC loss for Al_2O_3-layer insulated and not insulated cable samples measured at external field of 70 mT and frequencies 72 Hz and 144 Hz. One can see a small decrease of AC losses for insulated cable, which can be explained by lowered coupling loss component. Figure 13(b) compares Rc-B samples at 20 K in a wide range of frequency 2.3-104 Hz confirming the positive effect of cable oxidation on the total AC loss.

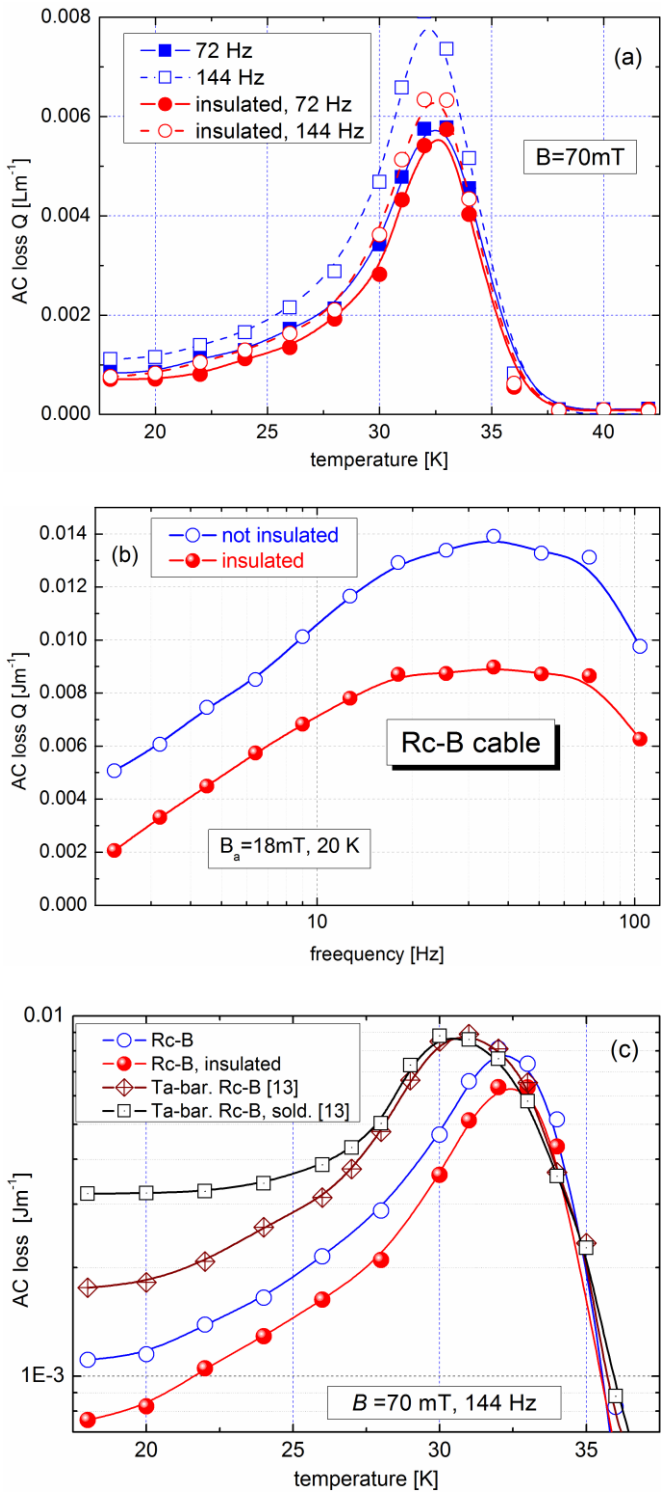

Figure 13. The AC losses of insulated by Al_2O_3 and not insulated Rutherford cable Rc-B versus temperature (a), frequency dependence measured at 20 K (b) and comparison with Ta barrier Rc-B cable (c).

Although the individual strands are better insulated by Al_2O_3 from outer side (~ 15 µm layer) and much less inside the cable (~ 3 µm layer), see Figure 12(d), reduced AC losses were clearly observed.

Similar Rutherford cable with Ta barrier (Rc-B-Ta) has been made and measured at the same range of temperature [13]. Figure 13(c) compares the AC losses at 144 Hz and 70 mT in semi-log plot for present Rc-B cable and Rc-B-Ta one with soldered and not soldered strands. Apparent are the differences of AC loss bellow 25 K, where coupling loss component is dominating and soldered strands show the largest values. Present Rc-B cable with Ti barrier has lower losses than Rc-B-Ta, which can be ascribed by lower barrier's resistivity, see Figure 14. While a similar $\rho \sim 2 \times 10^{-8}$ Ωm was measured for Ta and Al-B sheath [28] used for bough cables, by one order of magnitude higher resistivity of Ti barriers (> 2×10^{-7} Ωm) plays also a role of resistive barrier reducing the coupling currents inside the cable.

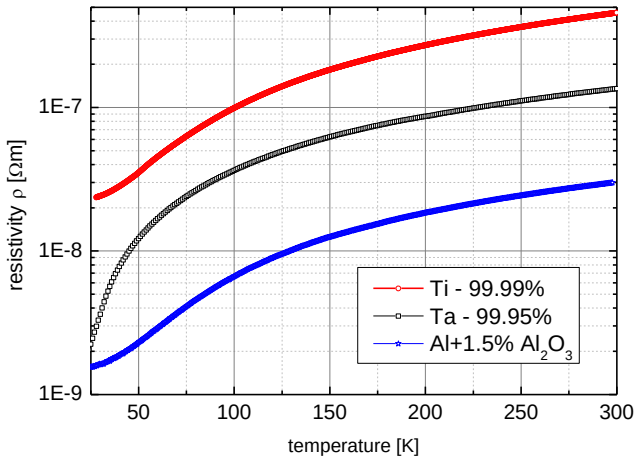

Figure 14. Resistivity of used Ti and Ta barriers and Al+1.5% Al_2O_3 sheath between 25 K and 300 K.

4. Conclusions

MgB_2 cables have been made of thin IMD wires (0.389-0.448 mm) with Cu and Al+Al_2O_3 sheaths. The rotary swaging deformation can increase critical currents of cables made of as-drawn IMD considerably due to more dense boron. The best $J_e(B)$ performance was obtained for the mechanically stronger Cu sheath. It was shown that the transversal and longitudinal non-uniformities affect the critical currents in MgB_2 strands made by IMD considerably. Consequently, observed non-uniformities show also the limit deformation for thin wires with Cu and Al+Al_2O_3 sheath. The propagation velocities of the quench measured along different Al+Al_2O_3 sheathed strands are similar but lower than Wilson and Dresner's predictions. The extra-light Rutherford cable with Ti barrier and Al+1.5% Al_2O_3 sheath allows effective reduction of the coupling current loss component due to increased barrier resistivity and also inter-strand resistivity enlarged by surface oxidation. It should be noted that further optimization of conductor fabrication and cabling process is still needed for the application of extra-light and low AC loss MgB_2 cable.

Acknowledgements

This work was supported by the Slovak Scientific Agency under projects APVV-18-0271, APVV-14-0719 and VEGA 2/0140/19. The authors acknowledge the financial support from MINECO-AEI-FEDER (project ENE2017-83669-C4-1) and from Gobierno de Aragón "Construyendo Europa desde Aragón" (research group T54_17R). Authors also would like to acknowledge the use of Servicio General de Apoyo a la Investigación-SAI, Universidad de Zaragoza.

References

[1] Kováč P et al 2010 *Supercond. Sci. Technol.* **23**, 105006
[2] Schlachter S. I et al 2006 *Physica C* **445–448** 777–783
[3] Haessler W et al 2013 *Supercond. Sci. Technol.* **26** 025005
[4] Higashikawa K et al 2014 *Physica* C **504** 62
[5] Kováč P et al 2018 *Supercond. Sci. Technol.* **21**, 125003
[6] Schlachter S. I et al 2010 *AIP Conference Proceedings* **1219** 302-309
[7] Holúbek T et al 2009 *Supercond. Sci. Technol*. **22**, 055011
[8] Kováč P et al 2010 *Supercond. Sci. Technol.* **23**, 105006
[9] Hušek I et al 2009 *Cryogenics* **49** 366–370
[10] Nosov A., 2019 *IEEE Trans on Appl Supercond* **29** 6200705
[11] Konstantopoulou K et al 2019 *Supercond. Sci.Technol.* **32** 085003
[12] Kopera L et al 2013 *Supercond. Sci. Technol*. **26**, 125007
[13] Kováč P et al 2018 *Sup Sci and Technology* **31** 015015
[14] Kováč J et al 2018 *Sup Sci and Technology* **31** 125014
[15] Balog M et al 2011 *Materials Science and Engineering A.* **529** 131-137
[16] Kováč P et al 2018 *Scientific Reports* **8** 11229
[17] Kováč P et al 2018 *Sup Sci and Technology* **31** 085003
[18] Cubero A et al 2018 *Supercond. Sci. Technol.* **31** 045009.
[19] Willering G P et al 2008 *J. Phys.: Conf. Ser.* **97** 012119
[20] Kováč J et al 2018 *Sup Sci and Technology* **31** 125014
[21] Seeber B 1998 Handbook of Applied Superconductivity (London: Institute of Physics Publishing) p 307
[22] Fabbricatore P et al 2003 *Sup Sci and Technology* **16** 364
[23] Kováč P et al *Sup Sci and Technology* 1997 **10** 605
[24] Hossain M et al 2014 *Sup. Sci. and Technology* **27** 095016
[25] Wilson M N 1983 Superconducting Magnets (Oxford: Clarendon)
[26] Pelegrín J et al 2013 *Supercond. Sci. Technol.* **26** 045002
[27] Dresner L 1995 Stability of Superconductors (Selected Topics in Superconductivity) (New York: Plenum)
[28] Kováč P et al 2017 *Cryogenics* **87** 58-65